Dynamics of Ce-O bond energy upon formation of O vacancies

Xuze Guan,†[1] Zhangyi Yao,†[1] Haoxin Liu,[2] Yonghui Liu,[3] Rong Han,[3] Lu Chen,[1] Deniz Wong,[4] Christian Schulz,[4] Hiroyuki Asakura,[5] Jie Zhang,[1] Shusaku Hayama,[7] Matthijs A. van Spronsen,[7] Yifei Ren,[1] Lun Zhang,[1] Xinlian Su,[1] Tsunehiro Tanaka,[6] Yuzheng Guo,*[3] Chunjiang Jia,*[2] Feng Ryan Wang,*[1]

[1.] Department of Chemical Engineering, University College London, Roberts Building, Torrington Place, London WC1E 7JE, UK

[2.] Key Laboratory for Colloid and Interface Chemistry, Key Laboratory of Special Aggregated Materials, School of Chemistry and Chemical Engineering, Shandong University, Jinan, 250100, China

[3.] School of Electrical Engineering and Automation, Wuhan University, Wuhan, China

[4.] Department of Dynamics and Transport in Quantum Materials, Helmholtz-Zentrum Berlin für Materialien und Energie, Hahn-Meitner-Platz 1, Berlin, Germany

[5.] Department of Applied Chemistry, Faculty of Science and Engineering, Kindai University 3-4-1, Kowakae, Higashi-Osaka, Osaka, 577-8502, Japan

[6.] Department of Molecular Engineering, Graduate School of Engineering, Kyoto University, Kyotodaigaku Katsura, Nishikyo-Ku, Kyoto 615-8510, Japan

[7.] Diamond Light Source, Harwell Science and Innovation Campus, Didcot, OX11 0DE, UK

† These authors contributed equally to this work.

* Corresponding author e-mail:

ryan.wang@ucl.ac.uk; jiacj@sdu.edu.cn; yguo@whu.edu.cn

Abstract

CeO_2 offers excellent oxygen storage capacity for catalysis and energy applications. It accommodates a surprising number of oxygen vacancies (V_O), yet the driving force and origin of these V_O are rarely discussed. Through a combination of *in situ* techniques and resonant inelastic X-ray scattering (RIXS), here, we discovered that upon formation of the V_O, the remaining Ce^{4+}-O^{2-} bond energy increases by at least 0.2 eV. Such an increase in the bond energy provides an additional enthalpy change (ΔH) in the reaction of V_O formation, stabilizes the reduced CeO_2 phase and explains why CeO_2 can host an extensive array of V_O. This work demonstrates that RIXS is effective in probing metal-oxygen bond energy, possibly under working conditions, which is an ideal method to quantify electronic structures with material performance.

Introduction

The unique Ce^{3+}/Ce^{4+} redox couple of CeO_2 is associated with the reversible formation of oxygen vacancies (V_O)[1,2]. As a result, CeO_2 is commonly used as catalyst support due to its excellent oxygen storage capacity (OSC) for applications such as emission control[3], CO_2 reduction[4-6], water-gas shift reaction[7], reforming processes[8], organic reactions[9] and oxidation chemistry[10,11]. The addition of isovalent non-reducible elements, such as Zr^{4+} cations, into the CeO_2 lattice, has been shown to improve its physico-chemical properties, including its thermal stability, OSC, and oxygen mobility in the solid framework[12]. In addition, adding active metals such as Cu and Pd can enhance the redox of CeO_2[2,13]. The synergetic electronic interactions between metal and ceria promote metal−oxygen bond weakening, facilitate oxygen desorption, and promote active site regeneration[13,14].

The reducibility of CeO_2 can be described as the cost of the formation of V_O. Unlike many transition metal oxides, it has been shown that the crystal structure of nonstoichiometric ceria remains stable even in the presence of a significant number of V_O[15]. This raises an interesting question: What stabilizes such a large amount of V_O? An aspect that is important and has received relatively little attention so far is how the V_O affect the subsequent removal of oxygen atoms. Most of the theoretical calculation focuses on the cost of removing the first oxygen atom from the interface, while this cost may significantly differ as the surface undergoes further reduction[16,17]. Ševčíková et al.[18] demonstrated that the occurrence of oxygen reverse spillover on Rh/CeO_2 depends on the oxidation state of the ceria substrate, while inhibited spillover was observed for reduced ceria (CeO_{2-x}). Despite all these efforts, an in-depth understanding of the dynamics of Ce-O bonds upon the formation of O vacancies is still missing. This directly relates to the activity and the chemical/structural behaviours. The study of the dynamics of Ce-O bonds contributes to the understanding of the easy formation of V_O of CeO_2.

Resonant inelastic X-ray scattering (RIXS) techniques represent a powerful and site-selective approach[19,20]. Rueff et al. investigated elemental Ce by 2p3d-RIXS directly subjected to high pressure to induce the γ-α transition[21]. Early Ce $M_{4,5}$-edge measurements of CeO_2 by Butorin et al. showed that RIXS is an effective method for determining charge excitation[22]. Herein, we present the results of a RIXS investigation of the evolution of Ce-O bond energy and the impact on the activity of such catalytic systems. In this regard, a complementary study of density functional theory (DFT), *in situ* X-ray absorption spectroscopy (XAS), *in situ* Raman, *in situ* high energy resolution fluorescence detected (HERFD)-XAS and RIXS have been applied to understand the electronic properties and redox of Ce species during reactions.

Results and discussion

DFT studies were undertaken to provide insight into the changes in the Ce-O bond after the formation of a V_O (Fig. 1a). The integrated crystal orbital Hamilton population (ICOHP) shows the contribution of a specific contact to the bond strength[23]. After the introduction of an O vacancy, the bond strength of the second shell $Ce^{4+}-O^{2-}$ becomes stronger (-0.85 eV to -1.00 eV) and the bond length (2.36 Å to 2.30 Å) becomes shorter than the primitive system. These results suggest that the formation of V_O strongly influences the nature of the remaining Ce^{4+}-O bond (strength and length). However, it is challenging to study the $Ce^{4+}-O^{2-}$ bonding at different Ce^{3+} ratios.

RIXS is a scattering process that involves the absorption and emission of coherent X-rays, resulting in a "photon-in-photon-out" interaction. This technique has gained significant popularity as an experimental probe due to its bulk sensitivity (more than 100 nm) and ability to provide element- and orbital-specific information[24]. In this study, we use Ce M-edge RIXS to obtain direct information on the electronic excitations just above the ground state from inelastic scattering, which cannot be obtained from the first-order process of core-level spectroscopy[24]. Briefly, the method exploits the selective resonant 3d-4f excitation in Ce^{3+} ($3d^{10}4f^1$) and Ce^{4+} ($3d^{10}4f^0$). By tuning the incident photon energy, obtained RIXS show the transition from the specific intermediate state to the final states.

The 3d-XAS of CeO_2 (Fig. 1b) has a main peak (~884 eV) and a satellite (~889 eV), which originates from the strong covalency hybridization between Ce 4f and O 2p states[25]. Figure 1c presents the total energy level scheme of CeO_2, which shows that the ground state corresponds to a bonding state between $4f^0$ and $4f^1\underline{v}$ configurations, where $\underline{v}$ represents a ligand hole as the result of ligand to metal electron transfer (from O^{2-} to Ce^{4+})[22,26]. The intermediate states include Ce_{4f}-O_{2p} bonding, antibonding, and nonbonding states between $3d^9f^1$ and $3d^94f^2\underline{v}$ configurations (Fig. 1c). In the RIXS, a Ce 3d electron is initially excited to the 4f states by absorbing an incident X-ray photon with energy hv. Subsequently, a radiative transition occurs where a 4f electron transitions to the 3d state by emitting an X-ray photon with energy hv'. In this process, if the final state is the same as the initial state (bonding state), the elastic component can be obtained. It also is possible to make a transition to both nonbonding and antibonding states in addition to the bonding state (Fig. 1c). Since, by comparing the hv and hv' (energy loss = hv - hv'), the strength of the covalency mixing between Ce 4f and O 2p states can be obtained without a core hole on the Ce site.
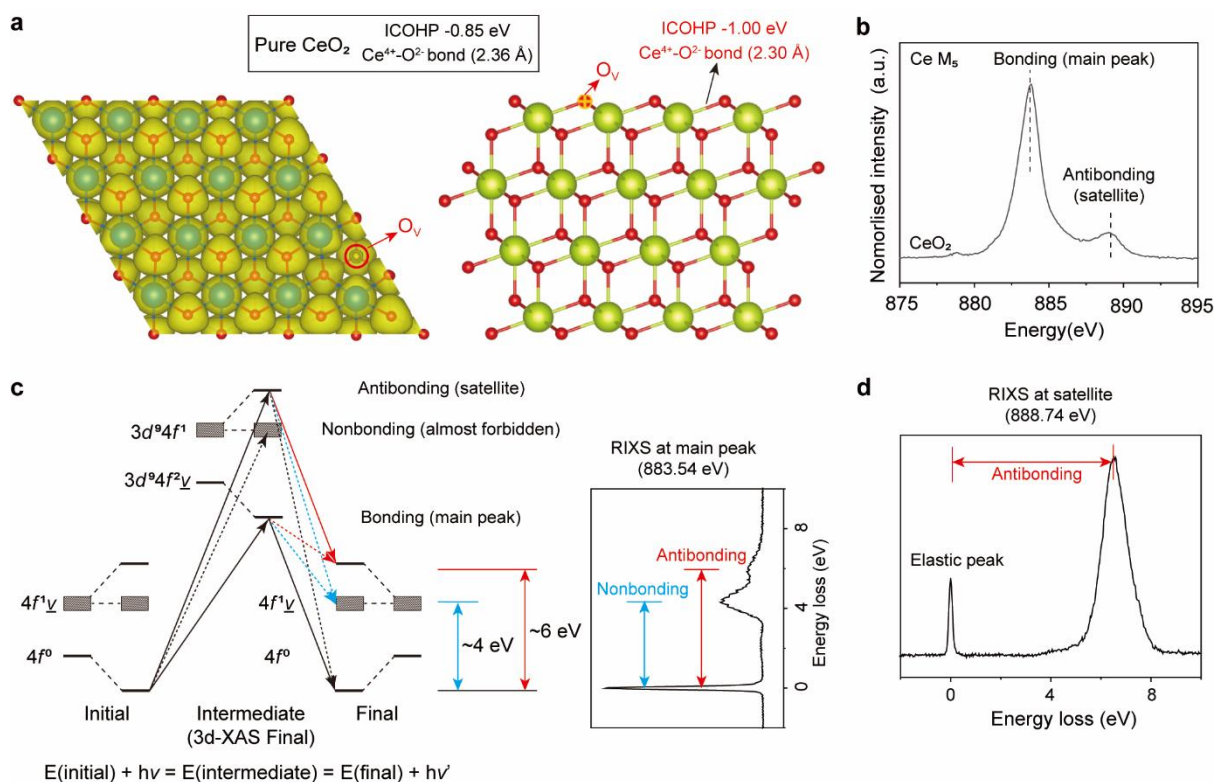

Figure 1. a, Top and side views of CeO_2 (111) surface with O vacancy and ICOHP of Ce^{4+}-O^{2-}

bond in pure CeO_2 and CeO_2 with O vacancy. **b,** XAS of Ce M_5-edge under O_2 at 300 °C. **c,** Total energy level scheme of $4f \rightarrow 3d$ RIXS for CeO_2, in which only the two lowest energy configurations are depicted for simplicity (see also ref. 22). The shaded rectangles denote the O 2p valence band. The transition is denoted by the arrow with solid lines (strong transition) and dash lines (weak transition). **d,** Energy loss at the excitation energy of 888.74 eV for CeO_2 under room temperature.

The RIXS spectra show a two-peak structure, where the relative intensity of the two peaks depends on the incident energy hv. When the incident energy is tuned to the main peak of 3d-XAS (883.54 eV), a strong transition to the bonding state and weaker transitions to nonbonding and antibonding states can be observed. The energy separation at about 4 eV corresponds to the distance between bonding and nonbonding states, while the energy separation at about 6 eV corresponds to the distance between bonding and antibonding states[27]. The satellite peak of Ce XAS is indicative of the contribution of $4f^0$ states as it arises from the transitions to 4f states in the conduction band[28]. When the incident energy is tuned to the satellite position of 3d-XAS (888.74 eV), the strong transition between the bonding and antibonding states of $4f^0$ and $4f^1\underline{v}$ configurations can be observed[29] (Fig. 1d).

To understand the properties of Ce-O bonds in Zr^{4+} doped catalysts and metal-modified catalysts, we synthesized and measured the 1wt% $Cu-CeO_2$ (CuCe), $Ce_{0.5}Zr_{0.5}O_2$ (CZ), 1wt% $Cu-Ce_{0.5}Zr_{0.5}O_2$ (CuCZ) and 1wt% $Pd-Ce_{0.5}Zr_{0.5}O_2$ (Pd-CZ) samples, characterization details are shown in Supplementary Figs. 1-6 and Supplementary Note 1. The commercial CeO_2 was used as a reference. The detailed RIXS spectra of as-synthesised samples and commercial CeO_2 are shown in Supplementary Figs. 7-14.

By excitation at 888.74 eV, the strong transition to the Ce^{4+} antibonding states can be measured. The energy separation between the bonding and antibonding states is mainly determined by the effect of hybridisation. To our surprise, Pd-CZ has the highest energy separation, while CeO_2 has the lowest energy separation (Fig. 2a). The separation between bonding and nonbonding states also follows this trend (Supplementary Fig. 15). This suggests that Pd-CZ has a stronger Ce^{4+}-O^{2-} bond than other samples. The inelastic peak position of antibonding states is positively correlated with the reactivity and reducibility of the catalyst. Considering ultra-high vacuum (UHV) is a reductive condition, the possible reason is that only stronger Ce^{4+}-O bonds can exist in highly reducible catalysts under reduction.

In the XAS spectra, the 881.6 eV feature is associated with Ce^{3+} (Fig. 2b). Exciting at 881.6 eV, a strong feature at 230 meV of energy transfer is observed for all samples (Fig. 2c). This feature is associated with the Ce^{3+} $4f^1$ state in the form of $^2F_{5/2} \rightarrow {}^2F_{7/2}$ transition (Fig. 2d). Ce^{4+}, on the other hand, should not have any feature at this energy range[26]. The ratio of the $^2F_{5/2} \rightarrow {}^2F_{7/2}$ peak to the elastic scattering peak gives an approximate indication of the Ce^{3+} content. Such ratio is in the order of Pd-CZ > Cu-CZ > CZ > CuCe > CeO_2, suggesting that both Zr doping and surface metal lead to higher Ce^{3+} concentration in the catalyst. The energy loss was found to be positively correlated with the ratio of Ce^{3+} (Fig. 2e). A higher concentration of Ce^{3+} increases the stress energy and shortens the Ce^{4+}-O^{2-} bond, resulting in a stronger Ce^{4+}-O bond.
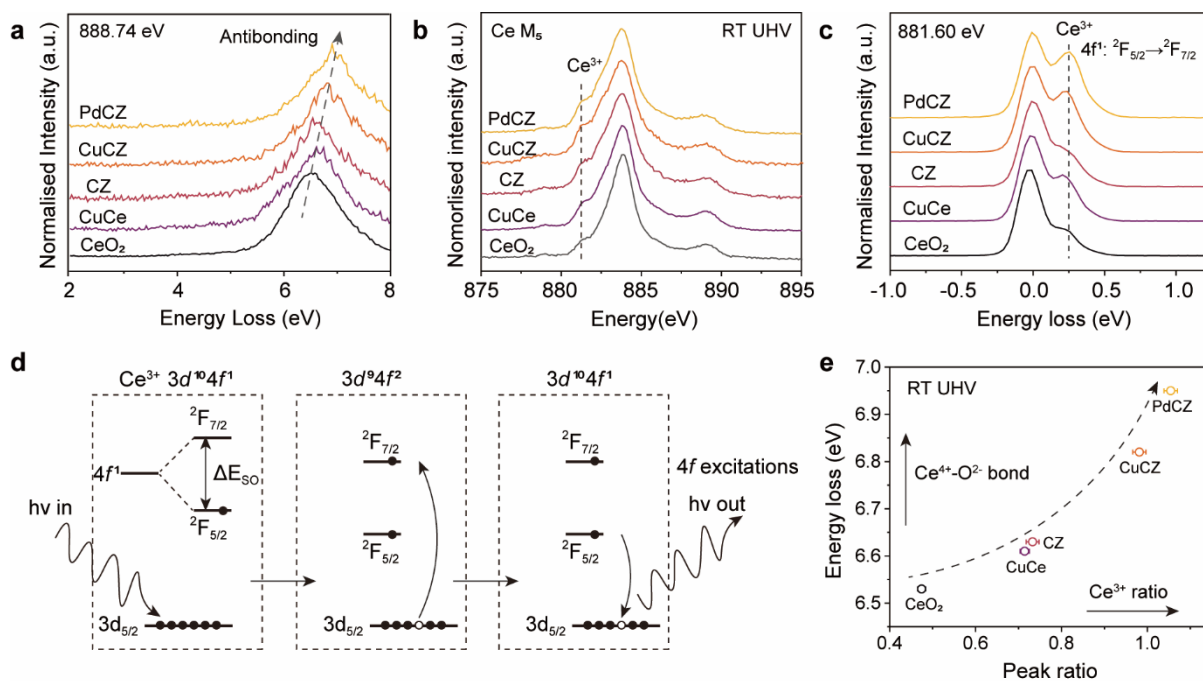
Figure 2. **a,** Energy loss at the excitation energy of 888.74 eV for various samples under UHV at room temperature. **b,** XAS of Ce M$_5$-edge for various samples under UHV at room temperature. **c,** Energy loss at the excitation energy of 881.60 eV for various samples under UHV at room temperature. **d,** Scheme of the spin-orbit splitting of the 4f states for a Ce^{3+} ion. **e,** Relationship between the energy separation and the peak ratio of the $^2F_{5/2} \rightarrow {}^2F_{7/2}$ peak to the elastic scattering peak.

By heating up under UHV, more Ce^{4+} in CZ is reduced to Ce^{3+}, as shown in Fig. 3a. The changes in O K-edge are shown and discussed in Supplementary Fig. 16 and Supplementary Note 2. With more Ce^{3+}, the energy loss for the antibonding states of Ce^{4+} is increased (Fig. 3b). It is noteworthy that the energy separation between bonding and antibonding states of CZ (6.80 eV) is 0.2 eV lower than that of Pd-CZ (7.00 eV) under the similar Ce^{3+} ratio. This is consistent with our speculation that the sample with higher antibonding states under reductive conditions has better redox behaviour, as the remaining Ce^{4+}-O^{2-} bond is strengthened during reduction. This means that breaking the Ce^{4+}-O^{2-} bond will become more difficult in reduced Pd-CZ. The stronger Ce^{4+}-O^{2-} bond suggests lower energy of final states, indicating a higher enthalpy change (ΔH) in the reaction to lose oxygen (Fig. 3c). The formation of O vacancies leads to entropy increase (ΔS). According to the Gibbs free energy formula ($\Delta G = \Delta H - T\Delta S$), the formation of O vacancies is favoured at high temperatures, with extra ΔH being thermodynamically more favourable. Therefore, we speculate that Pd-CZ has better redox behaviour and OSC.

Fig. 3d compares the OSC of the CeO$_2$, CZ and Pd-CZ catalysts at 300 °C. The reference sample, CeO$_2$ commercial particles, showed almost no OSC. The OSC performance of synthesized Pd-CZ was 5 times higher than that of CZ. To further clarify the redox behaviour of bulk and surface Ce in the CeO$_2$-based catalysts, *in situ* Ce L3 HERFD-XAS and near ambient pressure (NAP)-near edge X-ray absorption fine structure (NEXAFS) studies were conducted. HERFD-XAS is bulk sensitive. Under the reduction of CO, CeO$_2$ bulk remained

unchanged up to 300 °C (Fig. 3e, spectra in Supplementary Fig. 17). In contrast, the loading of Pd on the $Ce_{0.5}Zr_{0.5}O_2$ surface significantly promotes the reduction of Ce (Fig. 3f, spectra in Supplementary Fig. 18). The spectra of CuCe, CZ and CuCZ are shown in Supplementary Figs. 19 to 22 and further discussion is in Supplementary Note 3. *In situ* NAP-NEXAFS experiments further confirm the highest surface reducibility of Pd-CZ (Supplementary Fig. 23 and Supplementary Note 4).
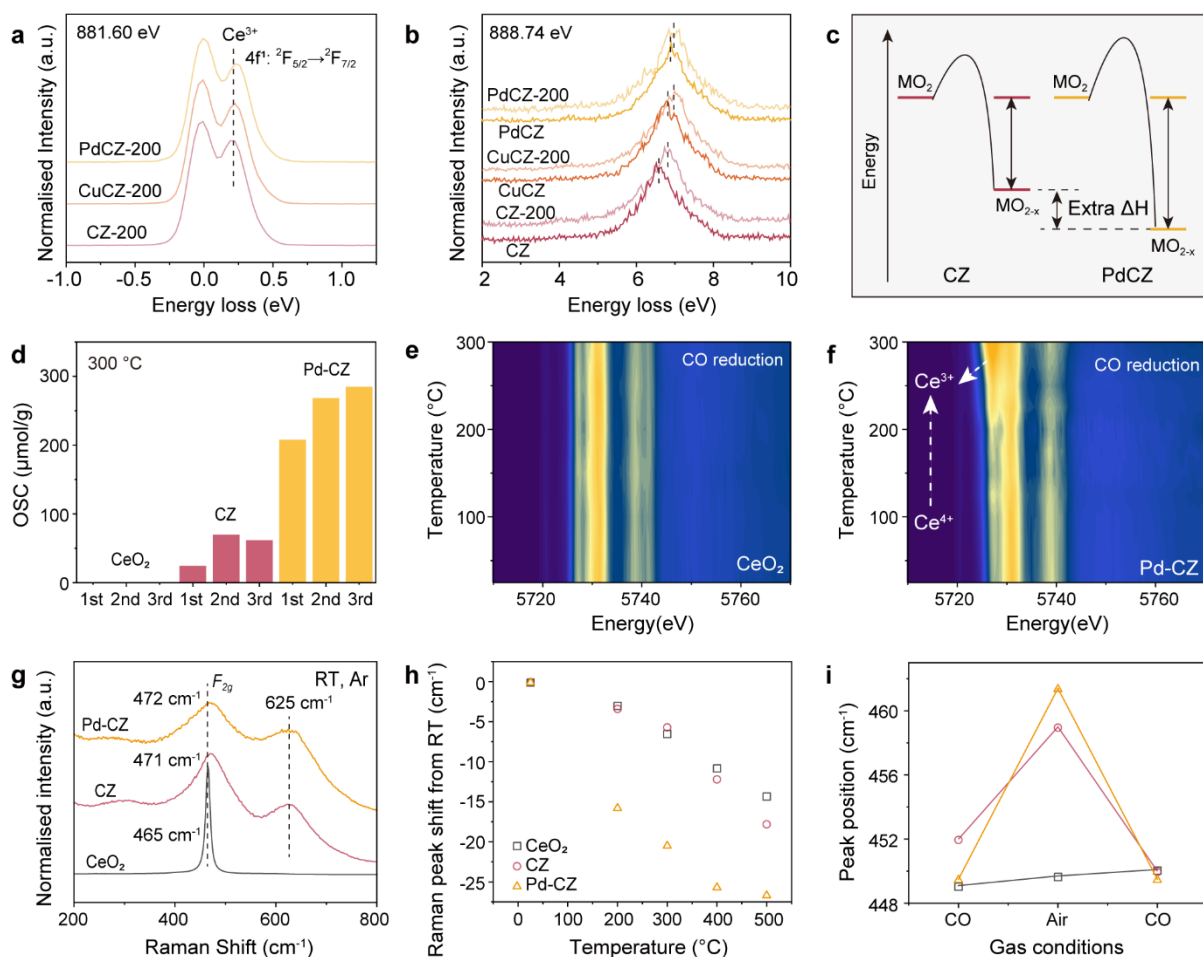

Figure 3. a, Energy loss at the excitation energy of 881.60 eV under UHV at 200 °C. **b,** Energy loss at the excitation energy of 887.74 eV under UHV at 200 °C. **c,** Simplified energy level diagram of the reduction of CZ and Pd-CZ. **d**, The oxygen storage capacity (OSC) of the as-synthesized CZ, Pd-CZ catalysts and CeO_2 commercial powder, respectively. **e,f,** *In situ* HERFD-XANES of (**e**) CeO_2 and (**f**) Pd-CZ in 2% CO from RT to 300 °C. **g,** Raman spectra of CeO_2, CZ and Pd-CZ under Ar at room temperature. **h,** Main CeO_2 Raman peak (F_{2g}) shifts (relative to the shifts at 25 °C) as a function of temperature during CO flow (5% CO in He) over commercial CeO_2, CZ and Pd-CZ. **i,** Changes in the F_{2g} peak position of commercial CeO_2, CZ and Pd-CZ with CO/Air switching at 500 °C. The Raman spectra were normalized to the peak height of the CeO_2 F_{2g} peak near 460 cm^{-1}.

Ex situ and *in situ* Raman spectra were performed to characterize the crystal structure of the catalysts. The CeO_2 sample showed one strong Raman peak at 465 cm^{-1} (F_{2g} mode of cubic CeO_2), which is usually reported relevant to a perfect ceria lattice at room temperature[30]. Its peak position varies with the length of Ce-O bonds in ceria-based catalysts[31]. Zr doping leads

to a blue shift (from 465 to 471 and 472 cm^{-1}) for the as-prepared CZ and Pd-CZ samples due to the substitution of Ce^{4+} cations (ionic radius 0.97 Å) by smaller Zr^{4+} cations (ionic radius 0.84 Å). The peak at 625 cm^{-1} of CZ and Pd-CZ samples is attributed to the presence of defective structure in CeO$_2$-ZrO$_2$ materials (Fig. 3g)[32].

In situ Raman under 5% CO from RT to 500 °C were measured and the results were shown in Supplementary Figs. 24 to 26. The decrease in Raman shift of CeO$_2$ by ~15 cm^{-1} from RT to 500 °C seen in many cases is due only to thermal expansion and phonon coupling and decay. Larger decreases in the Raman shift indicate more vacancies, because of the lattice of expansion that occurs when Ce^{4+} (0.97 Å) is replaced by Ce^{3+} (1.04 Å)[33]. CZ has a similar Raman peak shift with CeO$_2$ below 300 °C and shows higher peak shift at high temperatures, while Pd-CZ has the highest Raman peak shift (Fig. 3h). Switching of CO and air at 500 °C, the CeO$_2$ exhibit no obvious shift (Supplementary Figs. 24b), while both CZ and Pd-CZ show reversible shift (Supplementary Figs. 25b and 26b). Pd-CZ has the biggest difference in peak position between CO and air at 500 °C (Fig. 3i). The rapid formation of oxygen vacancies at low temperatures meant the Pd-CZ catalyst has a strong ability to form O$_2$.

By modulating the particle size of the CeZrO$_4$ support in Co/Ce-Zr catalysts, Hensen and colleagues observed reverse oxygen spillover (ROS) from the support during treatment in hydrogen, resulting in the generation of oxygen vacancies[34]. The bulk reduction of ceria, induced by the formation of Pd metal, has been reported as an indication of ROS[2,35], which has introduced novel avenues for enhancing the activity and stability of catalyst systems employing Ce-based supports, due to the exceptional oxygen mobility of ceria[36]. Surface metal can activate the lattice oxygen of the CeO$_2$ support and facilitate ROS at the M-O-Ce interface[2]. The formation of O vacancies in the bulk leads to an increase in the bond strength of the remaining bulk Ce^{4+}-O^{2-}, which explains the inhibited ROS for reduced ceria. For metal-supported catalysts, the ROS is only suppressed at a higher reduction (stronger bulk Ce^{4+}-O^{2-} bonds) due to the presence of active surface sites, leading to higher OSC.

Metal supported on cerium-zirconium-based oxides has been commercially used in three-way catalysts (TWC)[37]. Nitrous oxide (N$_2$O) is a secondary pollutant formed within the TWC[38] and will become regulated with the introduction of the EURO 7 emissions regulations. N$_2$O is a potent greenhouse gas and a major contributor to stratospheric ozone depletion[39,40]. The direct catalytic decomposition (2N$_2$O = 2N$_2$ + O$_2$) of N$_2$O is a promising remediation technology for reducing N$_2$O emissions. The decomposition of N$_2$O over the catalyst involved redox cycles of the Ce, and N$_2$O acted as an oxidizing agent to react with the V$_O$ created upon heating with the concomitant formation of molecular O$_2$[41]. Therefore, the N$_2$O decomposition reaction is used to evaluate the activity of V$_O$ for different samples.

When testing for the N$_2$O decomposition, the CeO$_2$ catalyst showed no activity at temperatures below 550 °C, whereas the Cu-CeO$_2$ catalyst showed a N$_2$O conversion of 37% at 550 °C. Compared with pure CeO$_2$, the addition of Zr^{4+} boosted performance remarkably, which is slightly higher than that of Cu-CeO$_2$. Loading Cu and Pd on the CeZrO$_2$ leads to higher reactivity so that the Pd-CZ catalyst achieved 97% N$_2$O conversion at 550 °C. The N$_2$O decomposition rate is in the order of Pd-CZ > Cu-CZ > CZ ≥ Cu-CeO$_2$ > CeO$_2$ (Fig. 4a), which follows the same trend of ability in forming V$_O$ (Fig. 2e).
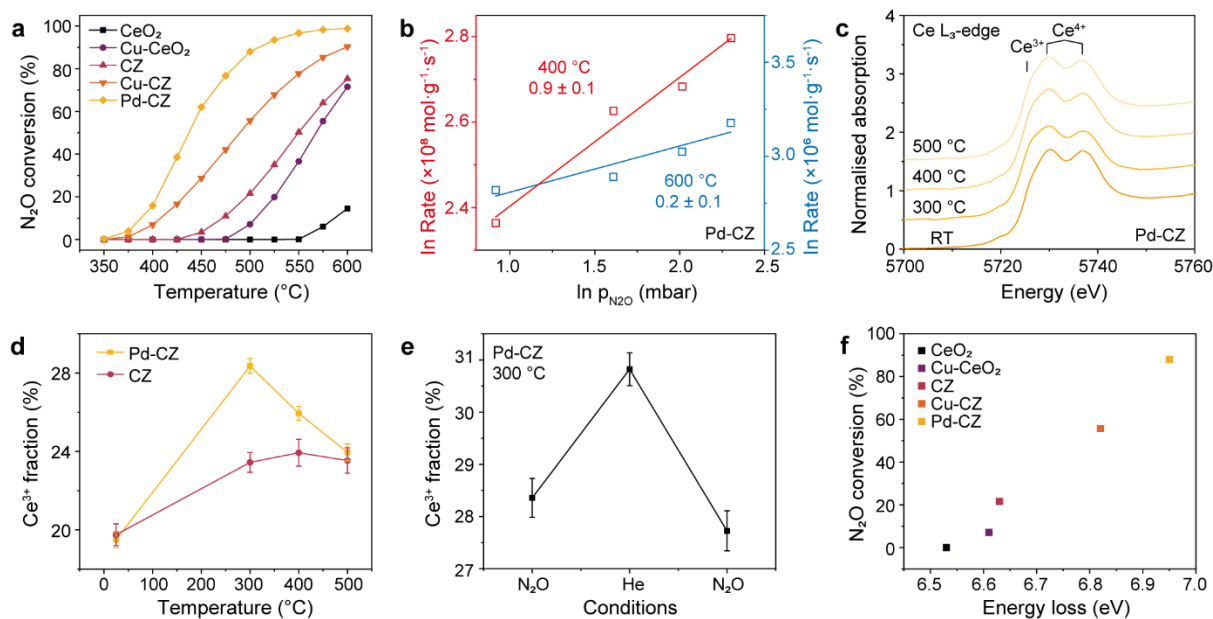
Figure 4. **a**, N_2O conversion as a function of temperature. **b**, Reaction order plots for the catalytic decomposition of N_2O over Pd-CZ, measured at 450 °C and 600 °C. 2-180 mg catalyst; total flow rate, 100 mL/min; and N_2O concentration, 0.25%-1% in He. **c**, Ce L_3-edge XANES spectra of Pd-CZ under various temperatures during N_2O decomposition. **d**, Ce^{3+} fraction in CZ and Pd-CZ as a function of temperature during N_2O decomposition reaction (2500 ppm N_2O, balanced in He). **e**, Ce^{3+} fraction in Pd-CZ under N_2O and He conditions at 300 °C. **f**, Relationship between N_2O conversion at 500 °C and the energy separation between bonding and antibonding states measured under UHV at RT.

The following mechanism of N_2O decomposition is generally accepted: (1) the extraction of the oxygen atom from N_2O ($N_2O + * \rightarrow N_2 + O*$) by the oxygen vacancy (*) of catalysts to yield N_2 and (2) the formation of molecular O_2 and O vacancies (*) ($O* + O* \rightarrow O_2 + 2*$ or $N_2O + O* \rightarrow N_2 + O_2 + *$) from the catalyst surface. Xiong et al. found that the splitting of N_2O (step 1) is the rate-determine step[42], while the formation of O_2 (step 2) is also reported as the rate-limiting step in the decomposition of N_2O[43,44]. Arrhenius plots were obtained in the applied temperature ranges of 380–420 °C and 560-600 °C (Supplementary Fig. 27). The Ea values were determined to be 117 kJ/mol in the lower temperature range and 67 kJ/mol under higher temperatures. The apparent reaction order decreased from 0.9 to 0.2 with increasing temperature (Fig. 4b), indicating that the activation of N_2O is easier at high temperatures.

To further clarify the reaction mechanism, especially the redox behaviour of Ce, *in situ* X-ray absorption near-edge spectroscopy (XANES) studies were conducted. Normalized Ce L_3-edge XANES spectra of the CZ catalyst and the Pd-CZ catalyst, measured *in situ* during the catalytic reaction of N_2O decomposition up to 500 °C, are shown in Figure 4c and Supplementary Fig. 28. To determine changes in the Ce oxidation state, a quantitative analysis was conducted by curve-fitting the XANES spectra using an arctangent function to simulate the edge jump and Gaussian functions for peak features[45] (Supplementary Fig. 29, fitting details in Supplementary Note 5).

At 300 °C, Ce^{4+} in both CZ and Pd-CZ can be reduced, while Pd-CZ has a higher Ce^{3+} concentration (Fig. 4d), showing that Pd-CZ is more prone to form V_O. Further, at 300 °C,

N$_2$O/He gas was introduced into the cell with an interval of He purge. Switching from N$_2$O/He to He, more Ce^{4+} is reduced (Fig. 4e). Then introducing N$_2$O, the Ce^{3+} fraction decreased to the origin state, suggesting that N$_2$O oxidized the Ce^{3+} species to form N$_2$. The increased Ce^{3+} ratios suggest that the breakage of the N-O bond (step 1) is the rate-limiting step at low temperatures. Raising temperature, Ce^{3+} in Pd-CZ can be gradually oxidized, whereas the Ce^{3+} fraction in CZ remains stable (Fig. 4d). With the oxidation of Ce^{3+}, N$_2$O has significant conversion in Pd-CZ, while CZ cannot convert N$_2$O during the reaction (Supplementary Fig. 30), indicating that the reactivity is related to the redox behaviour of Ce. At high temperatures, regeneration of the reduced active site can be considered to be the rate-limiting step since this coincides with O$_2$ formation[46]. The decreased Ce^{3+} ratios indicate that the formation of O vacancies (step 2) is the rate-determine step at high temperatures.

Surface metal species could act as activators for the migration and storage of oxygen on the support. Based on the dynamics of Ce-O bond energy at steady-state conditions, catalysts with high Ce^{3+} content (strong Ce-O bond) are favourable for oxygen spillover (OS), while catalysts with low Ce^{3+} content (weak Ce-O bond) favour ROS. Pd-CZ has a high concentration of Ce^{3+} under low temperatures and thus is prone to the dissociation of N-O bonds, showing lower light-off temperature. At rising temperatures, the Ce^{3+} in Pd-CZ is gradually oxidized, resulting in enhanced ROS, which is favourable for O$_2$ formation (regeneration of O vacancies) in N$_2$O decomposition. The evolution of remaining Ce^{4+}-O^{2-} bonds explains the special redox properties of CeO$_2$-based catalysts. The energy separation between bonding and antibonding states under reductive conditions can reflect the limit for support to lose lattice oxygen, which can serve as a key descriptor in catalysis. The N$_2$O conversion of different catalysts showed a positive correlation with their antibonding energies measured under UHV at RT (Fig. 4f). The enhanced reactivity is made possible due to the ability of the CeO$_2$ to adjust its bonding properties easily and drastically to best fit its immediate environment.

Conclusion

When V$_O$ is formed in the CeO$_2$ lattice, the remaining Ce^{4+}-O^{2-} bond energy increases and stabilizes the reduced lattice with such extra ΔH of the reduction reaction. This increase in bond energy explains the presence of a large amount of stabilised V$_O$ in CeO$_2$. Therefore, the antibonding states energy under reductive conditions is positively correlated with the reducibility and reactivity of the catalyst, serving as a descriptor in catalysis. The highest bond energy is achieved with the Pd-Ce$_{0.5}$Zr$_{0.5}$O$_2$ catalyst, which also has the highest activity in the N$_2$O decomposition reaction. The dynamics of Ce-O bond energy can be experimentally observed using RIXS, which can be applied to determine the M-O bond strength in other chemical systems.

Method

Sample preparation

Commercial CeO$_2$ (99.9%, CAS: 1306-38-3) was purchased from Acros Organics.

The 2wt% Cu-CeO$_2$ catalyst was obtained by conventional impregnation on CeO$_2$ nanospheres prepared by a microemulsion method as described in previous studies[47,48]. Firstly, 200ml n-

heptane, 8ml butanol and 8.87g triton X-100 were mixed in a 500ml 2-neck flask. The solution was sonicated for 10 minutes and then stirred for 30 minutes at room temperature to let them fully mix. Then 2 mL 0.5 M $Ce(NO_3)_3 \cdot 6H_2O$ solution ($Ce(NO_3)_3 \cdot 6H_2O$ 0.432 g + H_2O 2 mL) and 2mL 25% Trimethyl phenyl ammonium hydroxide solution (TMAH) was slowly added to the mixture with the colour changing from orange to yellow, then continuously stirred the mixture solution for 24 hours. After stirring, the formed yellow precipitate was collected by filtering and washing with MeOH three times. Then the solids were dried at 100 °C overnight with the colour changing from yellow to dark brown. The dark brown precipitate was calcined at 500 °C for 2 h (heating rate: 5 °C/min), and the colour changed back from dark to yellow. The obtained 550 mg yellow powder was stored in vacuum condition before loading Cu on it. The next step is loading 1 wt% Cu on CeO_2. 150mg obtained CeO_2 was added to 10 mL deionized water and sonicated for 30 mins to let it evenly disperse. A corresponding mass of $Cu(NO_3)_2 \cdot 2.5H_2O$ was added in CeO_2 dispersed solution as a precursor and then stirred for 10 mins. During this time, 250 mg Na_2CO_3 was dissolved in 5 mL deionized water and stirred for 10 minutes to obtain the Na_2CO_3 solution. Then, the Na_2CO_3 solution was added to the dispersed mixture and stirred for 2 h, followed by centrifugation (4000 rpm, 10 min) to remove the solution. The precipitate was washed with hot deionized water by reduced pressure filtration and then moved to the oven at 60°C overnight. Finally, using a train furnace system, the solid powder was reduced by 5% H_2 (balanced in Ar) at 250 °C for 1 h.

$Ce_{0.5}Zr_{0.5}O_2$ support was prepared by co-precipitation method by using cerium ammonium nitrate ($(NH_4)_2 \cdot [Ce(NO_3)_6]$), zirconium oxynitrate hydrate ($ZrO(NO_3)_2 \cdot xH_2O$) and ammonia hydroxide ($NH_3 \cdot H_2O$, 28%-30%) as precursors. 0.005 mol of ($(NH_4)_2 \cdot [Ce(NO_3)_6]$) and 0.005 mol of $ZrO(NO_3)_2 \cdot xH_2O$ were dissolved in 20 mL of deionized water. Subsequently, the mixture was stirred for 10 minutes, and then $NH_3 \cdot H_2O$ was added dropwise until pH reached 9 under continuous stirring. After stirring the mixture for 1 h, the obtained precipitation was filtered and thoroughly washed with deionized water to remove ammonium ions and then dried at 60 °C overnight. Then, the sample was carefully ground and calcined at 500 °C in the air for 2 h (heating rate: 5 °C/min).

The 1wt% Cu-CeZrO$_2$ and 1wt% Pd-CeZrO$_2$ catalysts were obtained by incipient wetness impregnation method by using copper nitrate trihydrate (0.25 ml solution for 1.0 g CeZrO$_2$) and palladium nitrate as precursors (0.25 ml solution for 1.0 g CeZrO$_2$). The Pd and Cu loading on the catalysts is 1wt%. After the impregnation, the samples were calcined in air at 500°C for 2 h (heating rate: 5 °C/min).

Catalytic performance

The decomposition of N_2O was evaluated in a fixed-bed flow system using a stainless-steel flow reactor (i.d. = 9.75 mm, 300 mm length). The composition and flow rate of the inlet gas mixture was set by the mass flow controller. A typical reaction gas composition was: 2500 ppm N_2O, balanced in He. The flow rate of the mixed gas was 100 mL/min. The catalyst was sieved below 250 µm of grain size. Typically, 200 mg of catalyst diluted in 200 mg SiC (400 mesh) was placed in the reaction tube, and the product was detected with the Quadrupole Mass Spectrometer (MS) Quantitative Gas Analyser (Hiden Analytical, UK). The reaction was studied in the temperature range of 350 °C to 600 °C. After reaching a steady state at each reaction temperature, the reaction was maintained for at least 30 minutes to measure the MS

signals of N_2O.

For both catalysts, the Ea and reaction order were measured with the same reactor for the catalytic performance described above. An appropriate amount of catalyst diluted with SiC was used, and the experiments were carried out by changing the temperature and gas flow rate, with the conversion within the kinetic regime.

Characterization

High-resolution aberration-corrected HAADF-STEM images were obtained from the probe-corrected (CEOS) JEM ARM 200CF (JEOL, Japan) operated at 200 keV. The samples for the analysis were dispersed in ethanol followed by the addition of a few drops of lacey carbon films supported on copper grids.

EDX data were obtained from the probe-corrected JEM ARM 200CF (JEOL, Japan) with large solid-angle dual EDS detectors for X-ray spectroscopy and elemental mapping. The EDS data acquisition was carried out in STEM imaging mode, with a probe current of 143 pA (probe size is 5 C) at 200 keV acceleration voltage. Gatan Microscopy Suite Software was used for EDS spectrum imaging data acquisition.

The measurement was performed on the STOE STADI-P diffractometer with a voltage of 40 kV at 30 mA, using a Cu source with $K_{\alpha 1} = 1.54060$ Å. With a resolution of 0.015° each step, the signals of 2θ in the range of 2°-80° were collected.

Electron paramagnetic resonance (EPR) measurements of $Cu-CeO_2$ and $Cu-CeZrO_2$ samples were carried out with an X-band Magnettech Bench-top ESR spectrometer MiniScope MS5000 under room temperature. Powder samples (~20 mg for $Cu-CeO_2$ and ~50 mg for Cu-CZ) were measured in a 4 m OD quartz EPR tube by sweeping the magnetic field between 100-500 mT under 10 mW microwave power (frequency 9.46 GHz). The field is modulated at 100 kHz frequency with 0.8 mT amplitude.

The oxygen storage capacities (OSCs) of all samples were obtained by a Builder PCSA-1000 instrument under the pulse mode. 50 mg of powder catalyst was pretreated under a gas flow of 20% O_2/N_2 (30 mL/min) at 200 ℃ (heating rate: 20 ℃/min) for 30 min. Under the same flow, the sample was heated to 300 ℃ with a rate of 20 ℃/min, followed by a purge of pure Ar (30 mL/min) to remove the residual oxygen. Then, the sample was treated with 5% H_2/Ar (30 mL/min) at 300 ℃ for 10 min, and flushed with pure Ar until the stabilization of baseline. After that, pure O_2 was pulsed into the reactor at 300 °C by several pulses at intervals of more than 1 min until the saturated adsorption of O_2. After the first round of testing, two more rounds of H_2 treatment-O_2 pulse testing were conducted. The O_2 volume of each pulse was 0.2 mL. The O_2-OSC values were determined by the amount of cumulative O_2 consumption during the O_2 pulses.

***In situ* XANES investigations**

The *in situ* XANES measurement was carried out in the BL01B1 beamline at Spring8 (Hyogo, Japan). The spectra were recorded in transmission mode with Si(111) double-crystal monochromator. The photon energy was calibrated at the inflexion point of the Ce L_3-edge XANES spectra of reference Ce foil (5723 eV). In the experiments, 2 mg of samples (CZ and Pd-CZ) were pressed into pellets with 58 mg boron nitride (diameter around 7 mm) and

measured in the *in situ* cell provided by BL01B1. The *in situ* XAS cell was equipped with a heater and thermocouples and sealed by a Kapton membrane. Products at the outlet of the reactor were analysed by a mass spectrometer (OmniStar), which was placed downstream. The X-ray beam was transmitted through the Kapton membrane and sample pellets were mounted in the cell. Ce L_3-edge XAFS spectra were acquired in a transmittance mode with a Quick XAFS system. *In situ* experiments were carried out by flowing a constant N_2O gas mixture (10 mL·min^{-1} with 2500 ppm N_2O, balanced in He) generated by mass flow controllers. The oxidation states of Ce under the condition of N_2O (2500 ppm N_2O, balanced in He) from room temperature to 500 ℃ were measured. At 300 ℃, the catalysts were measured under both N_2O conditions and pure He conditions with a total gas flow was 10 mL·min^{-1}. XANES under static conditions of each gas composition were recorded between 5510-6260 eV. The spectra processing and peak fitting analysis were processed with Athena[49]. The R-factor for peak fitting is below 0.001.

In situ HERFD-XANES investigations

HERFD-XANES and non-resonant XES measurements were carried out in the I20-Scanning beamline[50] at Diamond Light Source (DLS, UK). The incident beam energy was selected using a Si(111) 4-bounce scanning monochromator[51]. The X-ray emission spectrometer is equipped with three Si(642) spherical analysers, operated in the Johann configuration with a 1 m diameter Rowland circle[52]. The beam size (h×v) is 400 μm × 300 μm FWHM. For the *in-situ* measurement, catalyst powders were fixed inside the 3mm diameter Kapton tube to be measured from room temperature to 300 ℃. Samples were diluted with boron nitride to minimise self-absorption. Typically, 2 mg of catalyst was diluted with 50 mg boron nitride. The temperature is controlled by a thermocouple inserted into the catalytic bed.

In situ experiments were carried out by flowing different gas mixtures (15 mL·min^{-1} with 2% CO or 1% O_2 or 5% H_2, balanced in He) generated by mass flow controllers. The concentration of the respective gas was kept the same with balancing He while changing the composition of gas flow, which was monitored through a mass spectrometer connected to the outlet. CeO_2, $CeZrO_2$ (CZ), $Cu-CeO_2$, $Cu-CeZrO_2$ (Cu-CZ) and $Pd-CeZrO_2$ (Pd-CZ) samples were measured under reductive and oxidative conditions to study the redox behaviours of Ce: reduced form under CO, followed by pure He, and reoxidation under O_2 gas streams. The sequence of different atmospheres follows the order CO, He, O_2 to avoid interference. The spectra measurement always started after the stabilization of the gas flow. Under each condition, $L\alpha_1$ XES (3d → 2p) and several HERFD-XANES spectra were recorded until the catalysts reached stable states. For the *ex-situ* measurement, pellets were made for $Ce(NO_3)_3$·$6H_2O$ references with 13 mm die under 3-5 tons pressure for 1-1.5 min.

HERFD-XANES was measured at the peak of the $L\alpha_1$ emission line at 4840.0 eV, while scanning the incident energy between 5650-5900 eV with region-scan mode (edge region step = 0.3 eV). The spectra merging and normalization were processed with Athena[49]. Three repetitions (~20 min) were taken under each condition, making a total measurement time of 1 hour for each HERFD-XANES.

In situ NAP-NEXAFS investigations

In situ NAP-NEXAFS experiments for 1wt% $CuO-CeO_2$ were carried out at the VerSoX

beamline (B07-C) of Diamond Light Source[53] (DLS, UK). The beamline has a maximum $h\nu/\Delta(h\nu) > 5000$ with a photon flux $> 10^{10}$ photons s^{-1} from 170 eV to 2000 eV and can be operated (delivering lower flux) up to 2800 eV. Temperature control of the two available sample holders, all manipulator/analyser motions, and all endstation signals (sample current, analyser, diagnostics, etc.) are fully integrated in the EPICS and GDA controls and data acquisition environment of the beamline. The accuracy of the sample and analyser position is typically less than 10 µm. The gas pressure and composition are controlled *via* a butterfly valve and mass flow controllers. The endstation consists of a fixed interface flange that holds the entrance cone of the ambient-pressure electron energy analyser (SPECS Phoibos NAP-150). The samples (around 1 mg) were dispersed in water (around 1 mL) and dropped (around 2 droplets) on Au-coated Si (~1 cm × 1 cm), followed by heating at 70 °C to remove the solvent. NEXAFS spectra at Ce M_4/M_5 edge (875-915 eV) and O K-edge (520–560 eV) were measured in both total electron yield (TEY) mode and Auger electron yield (AEY) mode from room temperature to 300 °C. The measurements were performed either under UHV or various gas conditions (CO or O_2) with a total pressure of 1 mbar. The temperature was monitored by a K-type thermocouple and regulated by a PID controller.

In situ Raman investigations

Raman spectroscopy: *In situ* Raman spectra were measured by the LabRAM HR800 spectrometer (HORIBA JY) with an excited laser at 473 nm. The micro-Raman reaction cell (Xiamen TOPS) is equipped with a quartz window that has a heating module to control the test temperature. The powder catalysts were sealed in the *in situ* reactor for further Raman tests. The specific test programs were as follows:

The sample was purged by 20% O_2/N_2 (30 mL/min) at room temperature (RT) for 5 min and then heated to 200 ℃ (heating rate: 20 ℃/min) for 30 min. After that, the sample was cooled to RT under the pure Ar flow (30 mL/min) and then the gas flow was switched to 2% CO/Ar (30 mL/min) at RT. Under 2% CO/Ar atmosphere, the sample was heated from RT to 500 ℃ (heating rate: 20 ℃/min), and the Raman spectra were collected at RT, 200 ℃, 300 ℃, 400 ℃ and 500 ℃ after 10 min of steady-state reaction, respectively. After that, the sample underwent a consecutive switch of 20% O_2/N_2, 2% CO/Ar and 20% O_2/N_2. When the predetermined gas was introduced into the sample chamber, a period of 10 min was allowed for stabilization, followed by the signal collection. Finally, the temperature was cooled to RT and maintained for 10 min to collect Raman spectra.

XAS and RIXS investigations

Ce M-edge and O K-edge resonant inelastic X-ray scattering (RIXS) data of the catalysts were collected at the PEAXIS beamline[54,55] of synchrotron BESSY II at Helmholtz-Zentrum Berlin (HZB). The beamline delivers 1.4×10^{12} to 2.4×10^{11} flux at 400 eV and 4.6×10^{11} to 7.7×10^{10} flux at 900 eV. The focus size is 15 µm × 4 µm. A hemispherical energy analyser (SPECS PHOIBOS 150) is used for electron detections and a CCD camera (Andor iKon-L) is used for X-ray detections. We present here RIXS data taken from five samples (CeO_2, Cu-CeO_2, CZ, Cu-CZ and Pd-CZ). The sample powders were attached using Cu tape or conductive Ag paint. The scattering angle between the incident and scattered beam was constantly fixed at 90°. The O K-edge or Ce M-edge TFY (total fluorescence yield) of samples were first measured. For

RIXS experiments, Ce M-edge and O K-edge XAS spectra were used to select the incident excitation energy for the RIXS measurements. The samples were measured at room temperature and 200 °C under UHV. For temperatures above 300 K, the sample temperature is derived from the heating power, which currently restricts the precision to ±5 K below 350 K and above 700 K and to ±10 K in the intermediate temperature range. The final resolution was estimated to be ~70 meV for O K-edge and ~150 meV for Ce M-edge determined by the full width at the half-maximum (FWHM) coming from Gaussian fits at the elastic line. The data was processed by ADLER 4.0, a software designed for the PEAXIS Instrument.

DFT calculation

All spin-polarized DFT+U calculations were employed by Vienna Ab initio Simulation Package (VASP)[56]. The projector-augmented wave (PAW) method was performed to calculate the interaction between the ions and electrons. The exchange–correlation energy was handled by the Perdew-Burke-Ernzerhof functional[57]. A plane-wave basis set was employed with a cutoff energy of 400 eV. The 1×1×1 Monkhorst-Pack k-point grids were performed for all calculations. The energy and the force converged to 10^{-5} eV and 0.01 eV/Å, respectively. The van der Waals (vdW) interactions were handled by the DFT-D3 method[58]. The Coulomb interaction effect on screened Ce atoms was considered as U=4 eV and J=1 eV[59]. The thickness of the vacuum layer was set to 15 Å to weaken interactions the periodical interaction. The (100) surface of CeO_2 (111) was chosen as a result of its greater stability[60].

Data availability

Additional data can be found in the Supplementary Information. The data that support the findings of this study are available from the corresponding authors upon reasonable request.

References

1   Montini, T., Melchionna, M., Monai, M. & Fornasiero, P. Fundamentals and Catalytic Applications of CeO2-Based Materials. *Chem. Rev.* **116**, 5987-6041, doi:10.1021/acs.chemrev.5b00603 (2016).

2   Muravev, V. *et al.* Interface dynamics of Pd–CeO2 single-atom catalysts during CO oxidation. *Nat. Catal.* **4**, 469-478, doi:10.1038/s41929-021-00621-1 (2021).

3   Khivantsev, K. *et al.* Economizing on Precious Metals in Three-Way Catalysts: Thermally Stable and Highly Active Single-Atom Rhodium on Ceria for NO Abatement under Dry and Industrially Relevant Conditions**. *Angew. Chem.-Int. Edit.* **60**, 391-398, doi:10.1002/anie.202010815 (2021).

4   Wang, F. *et al.* Active Site Dependent Reaction Mechanism over Ru/CeO2 Catalyst toward CO2 Methanation. *J. Am. Chem. Soc.* **138**, 6298-6305, doi:10.1021/jacs.6b02762 (2016).

5   Zheng, K. *et al.* Ti-doped CeO2 Stabilized Single-Atom Rhodium Catalyst for Selective and Stable CO2 Hydrogenation to Ethanol. *Angew. Chem.-Int. Edit.* **61**, doi:10.1002/anie.202210991 (2022).

6   Xing, F., Nakaya, Y., Yasumura, S., Shimizu, K.-i. & Furukawa, S. Ternary platinum–

cobalt–indium nanoalloy on ceria as a highly efficient catalyst for the oxidative dehydrogenation of propane using CO2. *Nat. Catal.* **5**, 55-65, doi:10.1038/s41929-021-00730-x (2022).

7   Liu, H.-X. *et al.* Partially sintered copper–ceria as excellent catalyst for the high-temperature reverse water gas shift reaction. *Nature Communications* **13**, 867, doi:10.1038/s41467-022-28476-5 (2022).

8   Ay, H. & Üner, D. Dry reforming of methane over CeO2 supported Ni, Co and Ni–Co catalysts. *Applied Catalysis B: Environmental* **179**, 128-138, doi:https://doi.org/10.1016/j.apcatb.2015.05.013 (2015).

9   Kim, M., Su, Y. Q., Fukuoka, A., Hensen, E. J. M. & Nakajima, K. Aerobic Oxidation of 5-(Hydroxymethyl)furfural Cyclic Acetal Enables Selective Furan-2,5-dicarboxylic Acid Formation with CeO2-Supported Gold Catalyst. *Angew. Chem.-Int. Edit.* **57**, 8235-8239, doi:10.1002/anie.201805457 (2018).

10   Vincent, J. L. & Crozier, P. A. Atomic level fluxional behavior and activity of CeO2-supported Pt catalysts for CO oxidation. *NATURE COMMUNICATIONS* **12**, doi:10.1038/s41467-021-26047-8 (2021).

11   Muravev, V. *et al.* Operando Spectroscopy Unveils the Catalytic Role of Different Palladium Oxidation States in CO Oxidation on Pd/CeO2 Catalysts. *Angew. Chem.-Int. Edit.* **61**, doi:10.1002/anie.202200434 (2022).

12   Li, P., Chen, X., Li, Y. & Schwank, J. W. A review on oxygen storage capacity of CeO2-based materials: Influence factors, measurement techniques, and applications in reactions related to catalytic automotive emissions control. *Catal. Today* **327**, 90-115, doi:https://doi.org/10.1016/j.cattod.2018.05.059 (2019).

13   Kang, L. Q. *et al.* The Electrophilicity of Surface Carbon Species in the Redox Reactions of CuO-CeO2 Catalysts. *Angew. Chem.-Int. Edit.* **60**, 14420-14428, doi:10.1002/anie.202102570 (2021).

14   Zabilskiy, M., Djinović, P., Tchernychova, E. & Pintar, A. N2O decomposition over CuO/CeO2 catalyst: New insights into reaction mechanism and inhibiting action of H2O and NO by operando techniques. *Applied Catalysis B: Environmental* **197**, 146-158, doi:https://doi.org/10.1016/j.apcatb.2016.02.024 (2016).

15   Wu, L. *et al.* Oxidation state and lattice expansion of ${\mathrm{CeO}}_{2\ensuremath{-}x}$ nanoparticles as a function of particle size. *Phys. Rev. B* **69**, 125415, doi:10.1103/PhysRevB.69.125415 (2004).

16   Vecchietti, J. *et al.* Understanding the Role of Oxygen Vacancies in the Water Gas Shift Reaction on Ceria-Supported Platinum Catalysts. *ACS Catal.* **4**, 2088-2096, doi:10.1021/cs500323u (2014).

17   Ruiz Puigdollers, A., Schlexer, P., Tosoni, S. & Pacchioni, G. Increasing Oxide Reducibility: The Role of Metal/Oxide Interfaces in the Formation of Oxygen Vacancies. *ACS Catal.* **7**, 6493-6513, doi:10.1021/acscatal.7b01913 (2017).

18   Ševčíková, K. *et al.* Impact of Rh–CeOx interaction on CO oxidation mechanisms. *Appl. Surf. Sci.* **332**, 747-755, doi:https://doi.org/10.1016/j.apsusc.2015.01.197 (2015).

19   Glatzel, P. *et al.* The Electronic Structure of Mn in Oxides, Coordination Complexes, and the Oxygen-Evolving Complex of Photosystem II Studied by Resonant Inelastic X-ray Scattering. *J. Am. Chem. Soc.* **126**, 9946-9959, doi:10.1021/ja038579z (2004).

20   Chiogo, B. T. *et al.* Resonant inelastic x-ray scattering of spin-charge excitations in a Kondo system. *Phys. Rev. B* **106**, 075141, doi:10.1103/PhysRevB.106.075141 (2022).

21   Rueff, J. P. *et al.* Probing the $\ensuremath{\gamma}\mathrm{\text{\ensuremath{-}}}\ensuremath{\alpha}$ Transition in Bulk Ce under Pressure: A Direct Investigation by Resonant Inelastic X-Ray Scattering. *Physical Review Letters* **96**, 237403, doi:10.1103/PhysRevLett.96.237403 (2006).

22   Butorin, S. M. *et al.* Resonant X-Ray Fluorescence Spectroscopy of Correlated Systems: A Probe of Charge-Transfer Excitations. *Physical Review Letters* **77**, 574-577, doi:10.1103/PhysRevLett.77.574 (1996).

23   Fung, V., Wu, Z. & Jiang, D.-e. New Bonding Model of Radical Adsorbate on Lattice Oxygen of Perovskites. *The Journal of Physical Chemistry Letters* **9**, 6321-6325, doi:10.1021/acs.jpclett.8b02749 (2018).

24   Kotani, A. & Shin, S. Resonant inelastic x-ray scattering spectra for electrons in solids. *Reviews of Modern Physics* **73**, 203-246, doi:10.1103/RevModPhys.73.203 (2001).

25   Nakazawa, M., Tanaka, S., Uozumi, T. & Kotani, A. Theory of resonant X-ray emission spectra in Ce compounds. *J. Electron Spectrosc. Relat. Phenom.* **79**, 183-186, doi:https://doi.org/10.1016/0368-2048(96)02832-0 (1996).

26   Amorese, A. *et al.* $4f$ excitations in Ce Kondo lattices studied by resonant inelastic x-ray scattering. *Phys. Rev. B* **93**, 165134, doi:10.1103/PhysRevB.93.165134 (2016).

27   Nakazawa, M., Ogasawara, H. & Kotani, A. Theory of Polarization Dependence in Resonant X-Ray Emission Spectroscopy of Ce Compounds. *Journal of the Physical Society of Japan* **69**, 4071-4077, doi:10.1143/JPSJ.69.4071 (2000).

28   Kucheyev, S. O., Clapsaddle, B. J., Wang, Y. M., van Buuren, T. & Hamza, A. V. Electronic structure of nanoporous ceria from x-ray absorption spectroscopy and atomic multiplet calculations. *Phys. Rev. B* **76**, 235420, doi:10.1103/PhysRevB.76.235420 (2007).

29   Watanabe, M. *et al.* POLARIZATION DEPENDENCE OF RESONANT SOFT X-RAY EMISSION SPECTRA IN Ce COMPOUNDS. *Surface Review and Letters* **09**, 983-987, doi:10.1142/S0218625X02003184 (2002).

30   Andriopoulou, C. *et al.* Structural and Redox Properties of Ce1–xZrxO2−δ and Ce0.8Zr0.15RE0.05O2−δ (RE: La, Nd, Pr, Y) Solids Studied by High Temperature in Situ Raman Spectroscopy. *The Journal of Physical Chemistry C* **121**, 7931-7943, doi:10.1021/acs.jpcc.7b00515 (2017).

31   Xu, Y. *et al.* Resolving a Decade-Long Question of Oxygen Defects in Raman Spectra of Ceria-Based Catalysts at Atomic Level. *The Journal of Physical Chemistry C* **123**, 18889-18894, doi:10.1021/acs.jpcc.9b00633 (2019).

32   Si, R., Zhang, Y.-W., Li, S.-J., Lin, B.-X. & Yan, C.-H. Urea-Based Hydrothermally Derived Homogeneous Nanostructured Ce1-xZrxO2 (x = 0−0.8) Solid Solutions: A Strong Correlation between Oxygen Storage Capacity and Lattice Strain. *The Journal of Physical Chemistry B* **108**, 12481-12488, doi:10.1021/jp048084b (2004).

33   Lee, Y. *et al.* Raman Analysis of Mode Softening in Nanoparticle CeO2−δ and Au-CeO2−δ during CO Oxidation. *J. Am. Chem. Soc.* **133**, 12952-12955, doi:10.1021/ja204479j (2011).

34   Parastaev, A. *et al.* Boosting CO2 hydrogenation via size-dependent metal–support interactions in cobalt/ceria-based catalysts. *Nat. Catal.* **3**, 526-533, doi:10.1038/s41929-020-0459-4 (2020).

35   Vayssilov, G. N. *et al.* Support nanostructure boosts oxygen transfer to catalytically active platinum nanoparticles. *Nat. Mater.* **10**, 310-315, doi:10.1038/nmat2976 (2011).

36   Chen, J. *et al.* Reverse oxygen spillover triggered by CO adsorption on Sn-doped Pt/TiO2 for low-temperature CO oxidation. *Nature Communications* **14**, 3477, doi:10.1038/s41467-023-39226-6 (2023).

37   Nandi, S. *et al.* Relationship between design strategies of commercial three-way monolithic catalysts and their performances in realistic conditions. *Catal. Today* **384-386**, 122-132, doi:https://doi.org/10.1016/j.cattod.2021.05.005 (2022).

38   Wang, C. *et al.* Understanding ammonia and nitrous oxide formation in typical three-way catalysis during the catalyst warm-up period. *J. Hazard. Mater.* **438**, 129553, doi:https://doi.org/10.1016/j.jhazmat.2022.129553 (2022).

39   Strokal, M. & Kroeze, C. Nitrous oxide (N2O) emissions from human waste in 1970–2050. *Current Opinion in Environmental Sustainability* **9-10**, 108-121, doi:https://doi.org/10.1016/j.cosust.2014.09.008 (2014).

40   Wuebbles, D. J. Nitrous Oxide: No Laughing Matter. *Science* **326**, 56-57, doi:10.1126/science.1179571 (2009).

41   Jing, Y. *et al.* Catalytic Decomposition of N2O in the Presence of O2 through Redox of Rh Oxide in a RhOx/ZrO2 Catalyst. *ACS Catal.* **12**, 6325-6333, doi:10.1021/acscatal.2c01321 (2022).

42   Xiong, S. *et al.* Balance between Reducibility and N2O Adsorption Capacity for the N2O Decomposition: CuxCoy Catalysts as an Example. *Environmental Science & Technology* **53**, 10379-10386, doi:10.1021/acs.est.9b02892 (2019).

43   Lin, F. *et al.* Catalytic site requirements for N2O decomposition on Cu-, Co-, and Fe-SSZ-13 zeolites. *J. Catal.* **401**, 70-80, doi:https://doi.org/10.1016/j.jcat.2021.07.012 (2021).

44   Smeets, P. J. *et al.* The catalytic performance of Cu-containing zeolites in N2O decomposition and the influence of O2, NO and H2O on recombination of oxygen. *J. Catal.* **256**, 183-191, doi:https://doi.org/10.1016/j.jcat.2008.03.008 (2008).

45   Bianconi, A. *et al.* Specific intermediate-valence state of insulating 4f compounds detected by ${L}_{3}$ x-ray absorption. *Phys. Rev. B* **35**, 806-812, doi:10.1103/PhysRevB.35.806 (1987).

46   Wang, A. *et al.* Catalytic N2O decomposition and reduction by NH3 over Fe/Beta and Fe/SSZ-13 catalysts. *J. Catal.* **358**, 199-210, doi:https://doi.org/10.1016/j.jcat.2017.12.011 (2018).

47   Yao, S. Y. *et al.* Morphological effects of the nanostructured ceria support on the activity and stability of CuO/CeO2 catalysts for the water-gas shift reaction. *Physical Chemistry Chemical Physics* **16**, 17183-17195, doi:10.1039/C4CP02276A (2014).

48   Lin, L. *et al.* In Situ Characterization of Cu/CeO2 Nanocatalysts for CO2 Hydrogenation: Morphological Effects of Nanostructured Ceria on the Catalytic Activity. *The Journal of Physical Chemistry C* **122**, 12934-12943, doi:10.1021/acs.jpcc.8b03596 (2018).

49   Ravel, B. & Newville, M. ATHENA, ARTEMIS, HEPHAESTUS: data analysis for X-ray absorption spectroscopy using IFEFFIT. *J. Synchrot. Radiat.* **12**, 537-541, doi:10.1107/s0909049505012719 (2005).

50   Diaz-Moreno, S. *et al.* The Spectroscopy Village at Diamond Light Source. *J Synchrotron Radiat* **25**, 998-1009, doi:10.1107/s1600577518006173 (2018).

51   Hayama, S. *et al.* The scanning four-bounce monochromator for beamline I20 at the Diamond Light Source. *J Synchrotron Radiat* **25**, 1556-1564, doi:doi:10.1107/S1600577518008974 (2018).

52   Hayama, S. *et al.* Photon-in/photon-out spectroscopy at the I20-scanning beamline at diamond light source. *Journal of Physics: Condensed Matter* **33**, 284003, doi:10.1088/1361-648x/abfe93 (2021).

53   Held, G. *et al.* Ambient-pressure endstation of the Versatile Soft X-ray (VerSoX) beamline at Diamond Light Source. *J. Synchrot. Radiat.* **27**, 1153-1166, doi:10.1107/s1600577520009157 (2020).

54   Schulz, C. *et al.* Characterization of the soft X-ray spectrometer PEAXIS at BESSY II. *J. Synchrot. Radiat.* **27**, 238-249, doi:10.1107/S1600577519014887 (2020).

55   Lieutenant, K. *et al.* Design concept of the high-resolution end-station PEAXIS at BESSY II: Wide-Q-range RIXS and XPS measurements on solids, solutions, and interfaces. *J. Electron Spectrosc. Relat. Phenom.* **210**, 54-65, doi:https://doi.org/10.1016/j.elspec.2015.08.009 (2016).

56   Kresse, G. & Furthmüller, J. Efficiency of ab-initio total energy calculations for metals and semiconductors using a plane-wave basis set. *Computational Materials Science* **6**, 15-50, doi:https://doi.org/10.1016/0927-0256(96)00008-0 (1996).

57   Blöchl, P. E. Projector augmented-wave method. *Phys. Rev. B* **50**, 17953-17979, doi:10.1103/PhysRevB.50.17953 (1994).

58   Grimme, S. Semiempirical GGA-type density functional constructed with a long-range dispersion correction. *Journal of Computational Chemistry* **27**, 1787-1799, doi:https://doi.org/10.1002/jcc.20495 (2006).

59   Niu, H. *et al.* Revealing the oxygen reduction reaction activity origin of single atoms supported on g-C3N4 monolayers: a first-principles study. *J. Mater. Chem. A* **8**, 6555-6563, doi:10.1039/D0TA00794C (2020).

60   Torbrügge, S., Reichling, M., Ishiyama, A., Morita, S. & Custance, Ó. Evidence of Subsurface Oxygen Vacancy Ordering on Reduced ${\mathrm{CeO}}_{2}(111)$. *Physical Review Letters* **99**, 056101, doi:10.1103/PhysRevLett.99.056101 (2007).

Acknowledgement

We acknowledge Helmholz-Zentrum Berlin for the beamtime in BESSY II (222-11395ST). X.G. would like to thank the China Scholarship Council (CSC) for the PhD funding.

Author Contributions

† These authors contributed equally to this work.

F.R.W. supervised the study. X.G. and F.R.W. designed the experiments, analysed the results, and wrote the manuscript. Z.Y. carried out materials synthesis and catalytic evaluations. X.G. conducted the STEM measurement and the EPR study. X.G., Z.Y., D.W., C.S. and F.R.W. performed RIXS study. H.L. and C.J. performed OSC and *in situ* Raman analysis. Y.L., R.H. and Y.G. carried out the theoretical calculations. X.G., L.C., Z.Y., J.Z., X.S. and M.A.V.S. conducted the NAP-NEXAFS study. X.G., Z.Y., Y.R., S.H. and F.R.W. conducted the *in situ* HERFD-XANES measurement. L.Z. conducted the XRD measurement. Z.Y., H.A., T.T. and F.R.W. conducted the *in situ* XANES study.

Competing interests

The authors declare no competing interests.